DOI:
10.1016/j.jconrel.2016.07.005

Document Version
Peer reviewed version

Rapamycin/DiR Loaded Lipid-Polyaniline Nanoparticles for Dual-Modal Imaging Guided Enhanced Photothermal and Antiangiogenic Combination Therapy

Jinping Wang, Fang Guo, Meng Yu, Li Liu, Fengping Tan, Ran Yan, Nan Li

PII: S0168-3659(16)30430-8
DOI: doi: 10.1016/j.jconrel.2016.07.005
Reference: COREL 8362

To appear in: *Journal of Controlled Release*

Received date: 25 January 2016
Revised date: 12 June 2016
Accepted date: 2 July 2016

Please cite this article as: Jinping Wang, Fang Guo, Meng Yu, Li Liu, Fengping Tan, Ran Yan, Nan Li, Rapamycin/DiR Loaded Lipid-Polyaniline Nanoparticles for Dual-Modal Imaging Guided Enhanced Photothermal and Antiangiogenic Combination Therapy, *Journal of Controlled Release* (2016), doi: 10.1016/j.jconrel.2016.07.005

Rapamycin/DiR Loaded Lipid-Polyaniline Nanoparticles for Dual-Modal Imaging Guided Enhanced Photothermal and Antiangiogenic Combination Therapy

Jinping Wang [a], Fang Guo [a], Meng Yu [a], Li Liu[a], Fengping Tan [a], Ran Yan [b,] **, Nan Li [a,] *

[a] Tianjin Key Laboratory of Drug Delivery & High-Efficiency, School of Pharmaceutical Science and Technology, Tianjin University, Tianjin, PR China.

[b] Division of Imaging Sciences and Biomedical Engineering, King's College London, London, United Kingdom.

**Co-corresponding author at: Division of Imaging Sciences,The Rayne Institute, King's College London, 4th Floor, Lambeth Wing St Thomas' Hospital, London SE1 7EH, United Kingdom.

E-mail address: ran.yan@kcl.ac.uk

Tel: + 44-207-6792344

*Corresponding author at: School of Pharmaceutical Science and Technology, Tianjin University, 300072, Tianjin, PR China.

Tel.:+86-022-27404986

E-mail address: linan19850115@163.com

Abstract

Imaging-guided photothermal therapy (PTT) has promising application for treating tumors. Nevertheless, so far imaging-guided photothermal drug-delivery systems have been developed with limited success for tumor chemo-photothermal therapy. In this study, as the proof-of-concept, a stimuli-responsive tumor-targeting rapamycin/DiR loaded lipid-polyaniline nanoparticle (RDLPNP) for dual-modal imaging-guided enhanced PTT efficacy is reported for the first time. In this system, polyaniline (PANI) with π-π electronic conjugated system and effective photothermal efficiency is choosed as the appropriate model receptor of fluorescence resonance energy transfer (FRET), and loaded cyanine probe (e.g., 1,1-dioctadecyl-3,3,3,3-tetramethylindotri-carbocyanine iodide, DiR) acts as the donor of near-infrared fluorescence (NIRF). In addition, rapamycin (RAPA), which is used as the antiangiogenesis chemotherapeutic drug, can cutdown the tumor vessels and delay tumor growth obviously. After intravenous treatment of RDLPNPs into Hela tumor bearing mice, fluorescent (from DiR) and enhanced photoacoustic (from DLPNPs) signals were found in tumor site over time, which reached to peak at the 6 h time point. After irradiating with an NIR laser, a good anti-tumor effect was observed owing to the enhanced photothermal and antiangiogenic effect of RDLPNPs. These results show that the multifunctional nanoparticle can be used as a promising imaging-guided photothermal drug delivery nanoplatform for cancer therapy.

Keywords: Rapamycin, Lipid-polyaniline nanoparticles, Enhanced photothermal therapy, Antiangiogenesis, Imaging-guided therapy

1. Introduction

In the past decade, great efforts have been given to multifunctional nanomaterials that combine diagnostic and therapeutic functions for high-efficient and low-toxicity anticancer therapy. In particular, real-time imaging guided photothermal therapy (PTT) mediated by inorganic or organic nanoparticles responsive to near-infrared (NIR, λ = 700-1100 nm) light through conversion of photo energy into heat has attracted increasing interest due to its simplicity, safety, noninvasiveness as well as targeting and remote-control properties [1-4]. Therefore, studies in recent years have been designed to identify the most applicable PTT methods, extensively focusing on aspects such as controlling the shape of PTT agents [5, 6], developing novel materials [7-9], the fabrication process [10], using hybridization methods to enhance the PTT effect [11], and incorporating photoacoustic (PA) or fluorescence imaging reagents [12-14] and improving drug loading capabilities and release attributes [15].

Among various PTT agents, organic nanomaterials have attracted more attentions because the inorganic PTT materials usually are nonbiodegradable with cytotoxic properties and generally would remain in the body for long periods of time after systemic administration [16]. As an organic material, polyaniline (PANI) is potentially one of the most useful conductive polymers [17-20]. A distinct feature of PANI is that it can switch from the form of emeralidine base (EB) to emeralidine salt (ES) by doping protonic acids, alkali ions, or transition metals and so on ect., which can lead to strong NIR absorption and high conductivity [21]. Until very recently, several studies have reported that PANI nanoparticles can convert NIR light to thermo

energy. Thus, they can act as potential photothermal agents [21-23]. However, PANI nanoparticles alone have limited applications in cancer diagnosis and therapy due to low target to background contrast and poor tumor uptake [22, 24]. Therefore, additional effort is still needed to develop PANI nanomaterials with adequate PTT properties for efficient cancer therapy.

In spite of recent positive progress in the development of diverse photothermal materials [25, 26], there are only a few solutions to enhance the intrinsic photothermal property of PTT agents due to the lack of strategies to regulate their photothermal conversion efficiency except dimensions and concentrations [27, 28]. So far, the well-engineered photothermal agents for improving imaging guided PTT have not been reported [29-34], though stimuli-responsive nanomaterials are widely employed in the functional drug delivery system. Therefore, it is highly necessary to develop a multifunctional photothermal agent using as an efficient drug delivery system to improve the intrinsic photothermal performance and drug release capacity for imaging-guided enhanced PTT and chemotherapy.

Recently, great interests have been devoted to the NIR fluorescent dyes and their nanostructures for imaging guided PTT applications [35-41]. One representative example is the 1,1-dioctadecyl-3,3,3,3-tetramethylindotri-carbocyanine iodide (DiR) that is a lipophilic fluorescent probe (a subclass of cyanine dyes) with strong absorption in the NIR region and negligible cytotoxicity at low concentration suitable for both *in vivo* fluorescence imaging and photothermal treatment [42-44]. DiR has been developed as a particularly promising photothermal candidate because it can

convert absorbed fluorescent energy into heat via the non-radiative transition under the NIR laser irradiation. In addition, this type of cyanine dyes can also convert near-infrared fluorescence (NIRF) into thermal energy via radiative transition upon photoirradiation [14]. Due to this distinctive characteristic, the photothermal conversion efficiency of DiR is remarkably enhanced. Interestingly, PANI with π-π electronic conjugated system and broad NIR absorbance can act as a model receptor to receive the NIFR from a donor fluorescent probe such as DiR due to the fluorescence resonance energy transfer (FRET) effect [45]. Therefore, NIRF from DiR would be converted into additional thermal energy when coupled with the PANI nanoparticles to enhance their overall PTT.

In this work, as proof-of-concept, we designed a novel folic acid (FA)-grafted DiR loaded lipid-PANI nanoparticle (denoted as DLPNP) exhibiting FRET effect between DiR and PANI (Scheme 1a and b). The lipid-PANI nanoparticles with π-π electronic conjugated system and broad NIR absorbance is selected as a fluorescence resonance energy receptor and delivery system owing to its effective photothermal conversion efficiency, targeting ability and high drug loading capacity. DiR not only acts as the fluorescence resonance energy donor but also is used for NIR fluorescence imaging. In order to obtain a multifunctional nanoplatform applied simultaneously for PTT, NIR fluorescence imaging, chemotherapy and rapamycin (RAPA) which could inhibit primary and metastatic tumor growth by antiangiogenesis was encapsulated into DLPNPs to form the RAPA/DiR loaded lipid-PANI nanoparticles (RDLPNPs) (Scheme 1a and b). RDLPNP is hypothesized to accumulate in the tumor in a time

dependent manner and provides PA imaging in the tumor site. Additionally, although RDLPNPs exhibited FRET effect upon irradiation, there will be still some residual NIRF signals providing the whole body biodistribution of the RDLPNPs. In this study, both enhanced PA and fluorescence imaging are able to detect significant RDLPNPs tumor uptake. 6 h after RDLPNPs intravenous injection (i.v.), both enhanced PA and fluorescent signals reached peak intensity in the tumor, indicating high tumor uptake of RDLPNPs. Subsequently, PTT was conducted on Hela tumor xenograft bearing mouse model using RDLPNPs and therapeutic response was monitored over 48 days. Comparing with control groups, effective ablation of Hela tumors was achieved due to PTT induced RAPA release from the RDLPNPs. Our results proved the concept that RDLPNPs can be applied to the imaging guided combinational photothermal and chemo cancer therapy.

2. Materials and methods

2.1. Materials

RAPA was purchased from Seuss Tai Biotechnology co., Ltd. (Tianjin, China). Aniline was obtained from Aladdin biological technology co., Ltd. (Shanghai, China). Dodecylbenzene sulfonic acid (DBSA) was purchased from Huawei Cree Chemical Industry (Beijing, China). 1,1’-dioctadecyl-3,3,3’,3’-tetramethylindotricarbocyanine Iodide (DiR), and 3,3′-dioctadecyloxacarbocyanine perchlorate (DiO) were obtained from Mellon, Biological Technology co., Ltd. (Dalian, China). 1,2-Dipalmitoyl-sn-glycero-3-phosphocholine (DPPC),1,2-distearoyl-sn-glycero-3-phosphoethanolamine-N-[methoxy(polyethylene

glycol)-2000] (DSPE-PEG_{2000}), and folic acid conjugated 1,2-distearoyl-sn-glycero-3-phosphoethanolamine-N-[methoxy(polyethyleneglycol)-2000] (FA-DSPE-PEG_{2000}) were purchased from Shanghai Advanced Vehicle Technology Pharmaceutical Co., Ltd. (China). 3-[4,5-dimethylthiazol-2-yl]-2,5-diphenyl tetrazolium bromide (MTT), 4',6-diamidino-2-phenylindole (DAPI), dimethyl sulfoxide (DMSO), calcein acetoxymethyl ester (Calcein AM), and propidium iodide (PI) were obtained from sigma-Aldrich Co. LLC. (Beijing, China). All chemicals were of analytical grade and used without further purification.

2.2. Synthesis of emeraldine base PANI

The emeraldine base PANI was synthesized by chemical oxidation polymerization in the presence of excess hydrochloric acid (HCl). Aniline monomer (0.2 mol) was added to the 1M HCl aqueous solution (300 mL). Consecutively, the polymerization process was conducted by dropwise addition of ammonium persulfate (0.05 mol) solution prepared in 1M HCl aqueous solution (200 mL) as an oxidant and kept at 4℃ for 6 hours. The precipitated polymer salt was recovered from the reaction vessel by filtration. The obtained green precipitate was re-dispersed in a 1M sodium hydroxide solution (500 mL). Then the deprotonated emeraldine base PANI was filtrated and re-dispersed in acetone (500 mL). After filtration and dried in a vacuum oven for 48 hours, the emeraldine base PANI was obtained as fine purple powder. The yield of emeraldine base PANI powder from aniline monomer was about 69 wt%. The molecular weight of the synthesized emeraldine base PANI was

measured using gel permeation chromatography. In addition, absorbance of the prepared emeraldine base PANI was obtained using a Cary 60 UV-Vis spectrophotometer (Agilent, USA) and the characteristic bands were confirmed by Fourier-transform infrared spectroscopy (FT-IR, Varian, Excalibur™, USA).

2.3. Preparation of RDLPNPs

In this experiment, 5 mg of emeraldine base PANI (MW on a repeat unit basis = 93.128 g/mol) and 35.05 mg of DBSA was dissolved in 5 mL of chloroform. The resulting mixture was stirred for 24h to afford the emeraldine salt PANI that possesses the optical-absorbance peak in the NIR region and the long chain alkyl group. After adding 1 mL of the resulting polymer solution (1 mg PANI/mL, 10.7 µmol on a repeat unit basis) in a separate vial containing 20 mL of chloroform, the RAPA, 0.1 mg DiR (0.1µmol, MW = 1013.39 g/mol), 35.2 mg of DPPC (48.0 µmol, MW = 734.06 g/mol), 6.0 mg of DSPE-PEG_{2000} (2.0 µmol, MW = 2805.5 g/mol), and 1.4 mg of FA-DSPE-PEG_{2000} (0.4 µmol, MW = 3246.9 g/mol) were added and dissolved by ultrasonication for 2 min. The molar ratio of the polymer to the lipid was about 1:5. Then the solvent was evaporated at 50℃ at 120 rpm under reduced pressure using rotary film evaporator (Rotavapor, Buchi, Germany). The residual solvent was completely removed in vacuum at room temperature in 12 h. Finally, the thin film that formed on the inner wall of the vial was shattered to nanoparticles by adding 5 mL of phosphate-buffered saline (PBS, pH 7.4) and ultrasonicated for 5 min. The obtained nanoparticles were purified by centrifugation (10,000 rpm for 5 minutes). After that, the suspension was further purified by ultra-filtration through 100 kDa molecular

weight cut off (MWCO) filters. The obtained RDLPNPs could be readily re-dissolved in PBS and was stored for later use. The composition of all the nanoparticles used in this study was shown in the in Supporting Information Table S1. Drug loading efficiency and drug loading content were calculated according to the formulas:

$$\text{Drug loading efficiency} = \frac{\text{amounts of drug in nanoparticles}}{\text{total amount of drug}} \times 100\%$$

$$\text{Drug loading content} = \frac{\text{amount of drug in nanoparticles}}{\text{total weight of nanoparticles}} \times 100\%$$

To prepare the DiO-labeled DLPNPs, DiO instead of RAPA was extra added into the chloroform solvent. The other preparation process was the same as described above. The obtained DiO-labeled nanoparticles were dispersed in Dulbecco's modified Eagle medium (DMEM) and kept at 4 °C under darkness for confocal laser scanning imaging.

2.4. Characterization

The dynamic diameter of DLPNPs was determined by a Zetasizer Nano-ZS (Malvern Instruments, UK). UV-Vis spectra was measured by a Cary 60 UV-Vis spectrophotometer (Agilent, USA) using quartz cuvettes with an optical path of 1 cm. Fluorescence spectra of free DiR (in order to increase the solubility of free DiR, 1% Tween-80 was added into the aqueous solution), DLPNPs, and LPNPs in the aqueous solution were investigated by an LS-55 fluorescence spectrophotometer (Perkin-Elmer). Thermal images were captured by an SC300 infrared camera (Fluke TiR, USA) and analyzed by Examine infrared image software. The excitation source was an 808 nm diode-pumped solid-state laser system (LASERGLOW Technologies, Shanghai, China). The morphology and structure of DLPNPs before and after laser

irritation were characterized by the JEM-100 CX (Jeol Ltd., Tokyo, Japan) transmission electron microscopy (TEM).

2.5. In Vitro Release of RAPA from RDLPNPs

The amount of RAPA was measured by high performance liquid chromatography (HPLC) (Waters Corp., Milford, MA), using CLC-ODS-18 column (5 cm, 4.6 × 150 mm; Waters Corp., Milford, MA) maintained at 35 ℃,with an ultraviolet detector at 287 nm. An isocratic mobile phase of 10% water in 90% methanol (v/v) was used with a flow rate of 1 mL min^{-1}. The injection volume was 10 μL, and the retention time was about 5 min.

The drug release experiments were performed using the dialysis technique. An NIR laser with the wavelength of 808 nm (1.5 W) was employed in this work. RAPA-loaded nanoparticles (1 mL) with a final RAPA concentration of 0.72 mg/mL were placed into a dialysis tube with a molecular weight cut off of 3000 Da and dialyzed against 40 mL of PBS at pH 5.0 or 7.4 with 0.5% Tween-80 in a thermo controlled shaker with a stirring speed of 500 rpm at 37 ℃. Samples of 200 μL were withdrawn at specified times. RAPA concentration was determined by HPLC.

2.6. In Vitro Cellular Uptake and Chemo-photothermal Treatment

The Hela human cervical cancer cell line (originally obtained from American Type Culture Collection) and human umbilical vein endothelial cells (HUVECs) (obtained from Procell life science and technology co., Ltd. Wuhan, China) were used and cultured under recommended conditions. In the in vitro cellular uptake experiments, Hela cells or HUVECs (4×10^5 cells/well) were seeded into confocal

laser scanning microscopy (CLSM) culture dishes in 200 μL of medium for 24 h. For examining the intracellular uptake, Free DiO, free DiR or DiO labeled DLPNPs (100 μL) were added into different dishes respectively. After 6 h incubation, with the whole cells reaching about 80% confluence, the cells were washed with PBS three times and fixed with 4% paraformaldehyde solution for 20 min. Subsequently, the nuclei were stained with DAPI solution (5 μg mL^{-1} in PBS) for 10 min. The cells were rinsed with PBS three times and observed by CLSM (Leica Microsystems, Heidelberg, Germany). The Hela cells or HUVECs incubated with DiO-DLPNPs for 2 h and 4 h were exposed to 1.5 W cm^{-2} 808 nm laser irradiation for 3 min, respectively, and the cells were incubated for another 2 h and further investigated the photothermal influence on cellular uptake.

The in vitro cytotoxicity was measured using a standard methyl thiazolyltetrazolium (MTT, Sigma Aldrich) assay. For the MTT assay, Hela cells or HUVECs were seeded into 96-well cell culture plates with the number of 8000 per well until adherent and then incubated at a series of RAPA concentrations (i.e., 0, 1, 2.5, 5, 10, and 20 μg mL^{-1}) with various formulations of RDLPNPs and free RAPA for 24 h. For the photothermal experiment, the cells were treated with an 808 nm laser at a power density of 1.5 W cm^{-2} for 3 min. The standard MTT assay was carried out to determine the cell viabilities. In addition, in order to compare the cytotoxicity of different formulations, Hela cells or HUVECs were seeded into 96-well cell culture plates with the number of 8000 per well until adherent and then incubated with equivalent concentrations of PBS, free RAPA, LPNPs, DLPNPs and RDLPNPs (final

RAPA concentration 5 μg/mL, final PANI concentration 25 μg/mL) for 24 h. After 6 h, the cells treated with free RAPA, LPNPs, DLPNPs and RDLPNPs were irritated by an 808 nm laser at a power density of 1.5 W cm^{-2} for 3 min. After another 18 h incubation, the viability of cells was detected by the standard MTT assay.

For examining the chemotherapy and photothermal ablation for Hela cells or HUVECs in vitro, the cells (1×10^6 cells/well) were seeded into CLSM culture dishes in 200 μL of medium for 24 h. PBS and free RAPA (100 μL) were added into the dishes and then incubated for 6 h. The adherent cell solutions treated with DLPNPs and RDLPNPs were exposed to an 808 nm laser for 3 min with a power density of 1.5 W cm^{-2}. After removal of the medium, the adherent cells were washed with PBS for three times. Hela cells or HUVECs were incubated with calcein AM and PI solution for 15 min to separately stain the whole cells and dead cells. A green fluorescence color caused by calcein AM indicating viable cells and a red fluorescence color caused by PI indicating dead cells were then acquired by CLSM.

2.7. Animal Experiments

Female Balb/C mice were purchased from Beijing Huafukang Biological Technology Co. Ltd. and used under protocols approved by Tianjin University School of Pharmaceutical Science and Technology, Tianjin, China. Hela cells (1×10^6) suspended in 200 μL of PBS were subcutaneously injected into the oxter of each female Balb/C mouse. After ~10 days, the mice bearing Hela tumors were treated when the tumor volume reached ~80 mm^3. The mice were randomly divided into six groups (n = 5 per group) and treated under one of the following five experimental

conditions: i.v. injected with PBS only (PBS); i.v. injected with free RAPA only (Free RAPA); i.v. injected with RDLPNPs only (RDLPNPs); treated with LPNPs and exposed to the laser (LPNPs + NIR); treated with DLPNPs and exposed to the laser (DLPNPs + NIR); and treated with RDLPNPs and exposed to the laser (RDLPNPs + NIR). Tumor volumes were monitored every 2 days for 20 days. On day 8, major organs were collected after treatment and were formalin fixed and processed for routine hematoxylin and eosin (H&E) staining using standard methods. Images were collected using a Nikon light microscope (Nikon).

2.8. In Vivo Imaging and Biodistribution Analysis

In vivo fluorescent images of Balb/c mice were taken by using free DiR (dissolved in PBS with 10% ethanol) and DLPNPs. The mice were injected through the tail vein with 200 μL of free DiR and DLPNPs with the equivalent dose of 0.05 mg/kg DiR. The images were obtained by the ex/in vivo imaging system (CRi, Woburn, MA) with a 748 nm excitation wavelength and a 780 nm filter to collect the fluorescence signals of DiR at 0, 2, 4, 6 and 12 h. The mice after in vivo imaging were sacrificed and the tumors, hearts, livers, spleens, lungs, kidneys were collected for imaging and semiquatitative biodistribution analysis.

In vivo PA images of Balb/c mice were taken by using LPNPs and DLPNPs. The mice were injected through the tail vein with 200 μL of LPNPs and DLPNPs with the equivalent dose of 10 mg/kg PANI. After injection, PA images in the tumor sites were recorded on Vevo LAZR PAI System (808 nm) at 0, 2, 4, 6, and 12 h. Regions of interest (ROI) were drawn over the tumor, and the PA signal intensity was then carried

out using ImageJ.

2.9. In Vivo Infrared Thermal Imaging

Mice bearing Hela tumors treated with PBS, free RAPA, RAPA loaded LPNPs (RLPNPs), or RDLPNPs were irradiated with the 808 nm laser at power densities of 1.5 W cm^{-2} for 5 min and simultaneously imaged by an infrared thermal camera (Infrared Cameras. Inc.).

2.10. CD-31 Antibody Staining and Study of Nanoparticles' Penetration in Tumor

After tumor therapy experiment was complete, mice were respectively administered with PBS, free RAPA, DLPNPs and RDLPNPs, with or without NIR laser and were sacrificed 24 h post intravenous administration. Tumor was rapidly frozen at -80℃. Then, the treated tumor samples were sliced with a cryostat microtome. In order to observe the vasculature, the sections were incubated with a 1:250 dilution of CD-31 primary antibody at 4℃ overnight followed by incubation with Dylight 549-labeled secondary antibody (1:200) for 1 h at room temperature. The sections were also stained by DAPI and covered with a coverslip. The sections were observed using a confocal fluorescence microscope (Leica Microsystems, Heidelberg, Germany). Five randomly selected microscopic fields were quantitatively analyzed on ImageJ (National Institutes of Health).

2.11. Statistical Analysis

Results were expressed as mean ± standard deviation (SD). Two-tailed paired and unpaired Student’s t tests were used to determine differences within groups and between groups, respectively. P value <0.05 was considered statistically significant.

3. Results and discussion

3.1. Characterization of the DLPNPs

Polyaniline (PANI) was synthesized by using anilinium salts protonated by HCl and ammonium persulfate as an oxidant [46]. The chemical oxidative polymerization process was carried out at 4 ℃ for 6 hours to produce a dark-green precipitate, which was purified by washing with amounts of deionized water. This precipitate was dedoped by sodium hydroxide to obtain the purple polymer powder of emeralidine base PANI. The molecular weight of synthesized emeralidine base PANI was 5000 Da, as measured by gel permeation chromatography (polydispersity index: 1.2; Figure S1 in the Supporting Information). In the UV-Vis absorption spectra of emeralidine base PANI in chloroform, charge transfer between quinoid and benzenoid rings was observed at 580 nm (Figure S2 a in the Supporting Information). Furthermore, the chemical structure of emeraldine base PANI was confirmed by the FTIR spectra: 1156 cm^{-1} (N=Q=N vibrations: stretching vibrations of quinoid rings), 1301 cm^{-1} (aromatic C-N stretching), 1496 cm^{-1} (C=C and C=N stretching of benzenoid rings), and 1585 cm^{-1} (C=C and C=N stretching of quinoid rings; Figure S2 b in the Supporting Information). Then, the synthesized purple powder was dissolved in chloroform and re-doped by DBSA to obtain the emeralidine salt PANI (dark-green solution) with the long chain alkyl group. After adding the phospholipids (DPPC, DSPE-PEG_{2000}, FA-DSPE-PEG_{2000}) and DiR to above solution, the NIR dye loaded phase-separated thin film of PANI and phospholipids was obtained by evaporating the chloroform. The thin film was broken by ultrasonication after adding PBS (pH 7.4) to form

DLPNPs.

Transmission electron microscopy (TEM) image was used to detected the morphology of DLPNPs (Figure 1a). As shown in Figure 1c, the average size of DLPNPs was 140.6 nm with a polydispersity of 0.103. An intuitive comparison of DiR, PANI and DLPNPs was represented (Figure 1b). Free DiR and PANI were scarcely dispersed in water, whereas the as-prepared DLPNPs exhibited considerable water-solubility with a dark green color. To evaluate the stability, DLPNPs was dissolved in PBS and cell culture medium, respectively, and stored at 37 ℃ for 7 days. As shown in Supporting Information Figure S3 and Table S2, the appearance, sizes, polydispersity index (PDI), and the zeta potentials had no dramatic change. Figure 1d showed the UV-vis absorption spectrum of LPNPs, DLPNPs suspensions in PBS and free DIR dissolved in methanol, respectively. DLPNPs exhibited the absorbance peak at 754 nm, and fluorescence peak at 780 nm, confirming the successful incorporation of DLPNPs (Figure 1d and 1 e). When the DiR was encapsulated into the LPNPs, DLPNPs exhibited a great increase of absorbance from 600 nm to 810 nm (Figure 1d). In addition, such an increased absorption of DLPNPs in the NIR region ensured their potential application as the photothermal drug delivery carriers for NIR laser inducing chemo-photothermal therapy. To demonstrate that the attached dye fluorescence could be quenched by LPNPs via FRET, we measured the fluorescence intensities of DiR and DLPNPs. The DiR had showed strong fluorescence intensity in the aqueous solution. When it was encapsulated into LPNPs (forming DLPNPs), however, the attached dyes' fluorescence intensities

dropped significantly (Figure 1e). We further observed that DLPNPs had stronger fluorescence in methanol than that in water, suggesting that DLPNPs obviously quenched in aqueous solution, while recovered in methanol by reason of the high solubility of DiR in methanol (Figure S4 in the supporting information). Considering the observed dyes' fluorescence quenching, the decreased fluorescence intensity could be due to FRET between DiR molecules and PANI.

Considering that photostability greatly affected UV absorbance of cyanine dye, we investigated the ability of lipid-PANI nanoparticles to enhance the photostability of DiR. UV-Vis spectra showed that free DiR exhibited a decrease of absorbance under 808 nm photoirradiation within 10 min, which may due to its photobleaching (Figure 1f). DLPNPs only performed a little loss of absorbance under 754 nm photoirradiation during 10 min and still exhibited sufficient absorbance (Figure 1g). It indicated that LPNPs could significantly improve the photostability of DiR (Figure 1g), which was beneficial to the generation of photothermal energy or fluorescence from DiR. In addition, the stability of loaded DiR in the DLPNPs was also investigated. Only a negligible amount of free DiR was found in the medium (Figure S5, Supporting Information), indicating the good stability of DLPNPs.

In order to evaluate the enhanced photothermal effect of DLPNPs, we monitored the real-time temperature changes with NIR laser irradiation using the temperature gauge or infrared thermal imaging camera. Under the 808 nm laser irradiation at 1.5 Wcm^{-2} for 5min, the maximal temperature of DLPNPs, LPNPs, and free DiR reached to 62.8, 57.0, 36.3 ℃, respectively, while the temperature of PBS only increased by

8.2 ℃ (Figure 1h and i). Such a variation of DLPNPs could increase temperature over 50 ℃ after a short period of photoirradiation, which would cause an irreversible thermal ablation of cancer cells [47]. Remarkably, the temperature increase by DLPNPs was around 5 ℃ higher than that of LPNPs indicating additional thermal energy was generated by the FRET effect between DiR and PANI. These results also demonstrated that the broad absorbance of PANI enabled its absorption of most of fluorescence in the NIR region, thus maximizing the conversion efficiency of NIRF into thermal energy.

To investigate RAPA loading capacity of DLPNPs, different amounts of RAPA were loaded into PANI nanoparticles and loading efficiency was calculated (Figure 2a and b). When the amount of RAPA reached to 4.5 mg (the molar ratio of RAPA/PANI is 22.68), the drug loading efficiency decreased by 20%. Notably, less than 3.6 mg RAPA could be encapsulated into the DLPNPs. This was also the first time for RAPA encapsulation into DLPNPs, with much higher drug loading content than other current RAPA loaded formulations [48-50]. The drug release behavior of RDLPNPs and RLPNPs under different pH values were evaluated by dialyzing samples in either pH 5.0 or 7.4 PBS with 0.5% Tween-80 (Figure 2c and Figure S6 in the supporting information). Within 24 h, about 22% of RAPA was released from the RDLPNPs at pH 5.0, compared with 15% of that at pH 7.4, owing to the protonation of the amino group in the PANI molecule which might slightly change the structure of nanoparticles, thus facilitating drug release under acidic pH environment. In addition, the release behavior of RLPNPs was similar to that of LPNPs at pH 7.4 or pH 5.0.

Since the phase transition temperature of DPPC was 41.2 ℃ [51], we hypothesized that local heating of the nanocarriers might induce increased thermal vibration of lipid chains and thus weakened the binding with drug molecules. To prove the photothermal effect of DLPNPs on the RAPA release from the nanoparticles, RDLPNPs in PBS solutions with 0.5% Tween-80 at pH 5.0 or 7.4 were irradiated using an NIR laser (1.5 W cm^{-2} for 3 min, at 2, 6 and 24 h, respectively). The released RAPA before and after 808 nm laser irradiation was collected and measured by HPLC, in comparison to the samples in the dark without laser irradiation (Figure 2c and d). During the first 24 h, 38.6% of RAPA was released from the RDLPNPs, and increased to 94% of RAPA could release within 96 h. The data indicated that RAPA release from the RDLPNPs could be triggered by an NIR laser, likely due to the loosening of lipid-PANI packing resulting from a rapid local temperature increase. However, the amount of RAPA release from the RLPNPs was smaller than that of RDLPNPs due to the weak photothermal effect of the LPNPs. More interestingly, such photothermal-response release processes would depend on the environmental pH value. Significant NIR-triggered burst release of RAPA from RDLPNPS was noticed under acidic pH (pH = 5.0). In contrast, limited RAPA release was observed under physiological pH (pH = 7.4) even after exposure to the NIR laser irradiation. While being stable without NIR-triggered drug release outside cells under pH 7.4, RDLPNPS might release drug under NIR laser irritation only after entering tumor cells, where the pH value was about 5.0, minimizing the unnecessary drug release before cell internalization of nanoparticles.

3.2. In Vitro Cellular Uptake and Chemo-photothermal Treatment

To examine the intracellular uptake, DiO encapsulated DLPNPs were used for fluorescence detection (DiO was the substitute of RAPA). The subcellular localization of free DiO, free DiR, DiO-DLPNPs in Hela cells and HUVECs was investigated using confocal microscopy. After 6 h incubation with free DiO, only a little amount of DiO was observed in the nucleus of both Hela cells and HUVECs (Figure 3a). Despite there were still some residual DiR signals from DLPNPs in the Hela cells and HUVECs, the red signal from DLPNPs was weaker than that from free DiR, indicating that the NIFR was quenched owing to FRET from DiR to PANI. After treatment with the DiO-DLPNPs, however, both DiO and DiR signals of Hela cells were stronger than that of HUVECs. The increased cellular localization of DiO and DiR in Hela cells could be due to the highly overexpressed of FA receptors on Hela cells' surface [52]. To further confirm the ability of those particles to target the FA receptor, the competitive binding of non-FA functionalized DLPNPs (Non-FA-DLPNPs) and DLPNPs to Hela cells or HUVECs was performed by adding excess of free folate (1 mM) to block folate receptor binding 1 h before treatment with nanoparticles, respectively. The results (Figure S8 b and c) suggested the cellular uptake of DLPNPs decreased significantly in the presence of free FA in Hela cells, becoming almost equivalent to that of non-FA functionalized DLPNPs. However, neither the presence or absence of free FA in the culture medium influenced the cellular uptake of DLPNPs by HUVECs. It was clear that the selectivity of DLPNPs to Hela cells was blocked by free FA. Notably, DiO-DLPNPs formulation with NIR

laser not only significantly increased the fluorescence signals of DiO in both Hela cells and HUVECs, but also facilitated them entry into the nuclei (Figure 3a). In previous reports from others, it has been revealed that a proper thermal heating could increase the cell membrane permeability without damaging cells, improving the intracellular delivery of drugs [53, 54]. In addition, the heat caused by NIR laser could also induce the thermal vibration of lipid chains of DiO-DLPNPs and thus released more DiO into the cells and nuclei. Considering these factors, it is not surprising that photothermal heating significantly increased the uptake of DiO in both Hela cells and HUVECs.

Next, we tested the cell-killing efficacy of different RAPA formulations in vitro. In this study, Hela cells and HUVECs were incubated with free RAPA (dissolved in PBS containing 0.5% Tween-80) and RDLPNPs for 24 h, respectively. The RDLPNPs treated cells were irritated by an NIR laser (808 nm, 1.5 W cm^{-2}, 3 min). The relative cell viabilities were measured by the MTT assay and the results were shown in Figure S7. It was found that greater cytotoxicity was induced by higher drug level. At the same drug concentration, it was noted that the RDLPNPs with or without NIR laser significantly decreased the cell survival rate than that of the free RAPA. These results were attributed to the enhanced intracellular RAPA concentration facilitated by the RDLPNPs-mediated cellular uptake. In addition, the cytotoxic effect of chemotherapy, photothermal therapy, and chemo-photothermal therapy on Hela cells and HUVECs treated with PBS, free RAPA, DLPNPs, or RDLPNPs was evaluated respectively (Figure 3b). Without NIR laser irradiation, the viability of Hela cells and HUVECs

treated with DLPNPs was maintained at high rate, confirming that the DLPNPs were virtually nontoxic to Hela cells and HUVECs. Treated with free RAPA (5 μg/mL), however, the cell viability of Hela cells and HUVEC was decreased to 68.3 and 64.5%, respectively, indicating that the RAPA could inhibit the mammalian target of rapamycin (mTOR) pathway and lead to Hela cell and HUVEC death. In addition, the viability of Hela cells and HUVEC in the free RAPA plus NIR laser group was slightly lower than that in free RAPA group, revealing that free RAPA could not produce the photothermal effect under the NIR laser irradiation. Notably, upon NIR irradiation, the cytotoxicity of DLPNPs and RDLPNPs exhibited much pronouncedly increase than that of free RAPA. As the NIR laser irradiation alone did not lead to a decline in Hela cell and HUVEC viability, the observed increase in cytotoxicity could be attributed to the NIR irradiation-induced photothermal ablation and RAPA release mediated by RDLPNPs.

Similar results were also observed in the fluorescence staining of live/dead cells, where most of Hela cells and HUVECs incubated with RDLPNPs plus NIR irradiation presented PI-positive staining due to extensive cell death (Figure 3c). The results could be attributed to the following two reasons: Firstly, RDLPNPs were presumably internalized by cells in a more effective FA receptors mediated manner, leading to (1) a higher intracellular RAPA concentration comparing with free RAPA; (2) sufficient amount of PANI which preserved a profound phototriggered ablation effect. Secondly, RDLPNPs with the NIR laser irradiation produced the photothermal heating, which induced more RAPA release from DLPNPs as well as increased the

cell membrane permeability of RAPA. On the basis of these findings, it could be concluded that the RDLPNPs developed in this work were promising for antiangiogenesis and photothermal tumor ablation.

3.3. In Vivo Fluorescence and Photoacoustic Imaging

We then studied the in vivo biodistribution and tumor selectivity of DLPNPs on a subcutaneous (s.c.) Hela tumor model. Free DiR or DLPNPs (0.05 mg DiR/kg) were intravenously (i.v.) administered, and fluorescence images were acquired at different time points postinjection. Excitation and emission wavelengths were set as 745/780 nm for DiR. After injection, the mice were imaged with a Maestro EX in vivo fluorescence imaging system (CRi, Inc.) at 0, 2, 4, 6 and 12 h. From the results in Figure 4a, we could find that DLPNPs tended to be enriched in the tumor site over time, with the maximum uptake of nanoparticles in the tumor at 6 h. Control group revealed that the majority of free DiR was found in the liver and kidneys, suggesting selective tumor targeting by DLPNPs. The ex vivo fluorescent images of excised tissues further confirmed much higher accumulation of DLPNPs compared to free DiR in tumors (Figure 4b). No obvious fluorescence signals were observed in the heart, liver, spleen, lung and kidneys when treated with DLPNPs, while a dramatic accumulation of DiR was located in the liver and kidneys treated with free DiR (Figure 4b). Semi-quantitative analysis of biodistribution in various tissues revealed that the tumor accumulation of DLPNPs was 3.76-fold higher than that of free DiR at 12 h (Figure 4c). These results demonstrated that DLPNPs could be significantly enriched into tumor region by the enhanced active targeting and photothermal effect

in the animal model.

Compared to NIR fluorescent imaging, photoacoustics (PA) imaging was a newly developed biomedical imaging modality with increased imaging depth and improved resolution that had attracted great interest recently. It was developed on the base of PA effect of certain materials with strong light absorbance. Although optical imaging allowed whole-body imaging, PA imaging was especially helpful to visualize the distribution of imaging agent at tumor site. We applied PA imaging to observe the DLPNPs distribution in the tumor area. As shown in Figure 4d and e, the PA contrast at the tumor site gradually increased over time (609 ± 27, 1060 ± 56, 1850 ± 32 at 2, 4, 6 h, respectively) comparing to that before injection (350 ± 24 at 0 h). The PA contrast decreased to 970 ± 57 due to the clearance of DLPNPs in vivo at 12 h post injection. Comparatively, upon injection (6 h), substantial PA signals were mainly enriched in the inner of the tumor and the tumor site of even deep to 8 mm could be clearly detected. These results indicated that DLPNPs could penetrate into the innersection of the tumor, which could result from the active targeting effect of the nanoparticles. Once DLPNPs was penetrated into the tumor tissue, it could generate substantial amount of thermal energy upon NIR irradiation. Moreover, when LPNPs without DiR was injected, only a slight increase of PA signal was observed due to the lack of FRET effect between DiR and PANI. These results indicated the FRET effect could also enhance the PA signals. Finally, our fluorescence and photoacoustic imaging results suggested that DLPNPs-mediated PTT should be carried out at 6 h post injection due to the maximum accumulation of DLPNPs in the tumor area at this

time point.

3.4. In Vivo Photothermal Imaging

To monitor the in vivo photothermal effect generated by RDLPNPs, an infrared thermal mapping apparatus was used. After 6 h intravenously injection of PBS, free RAPA, RLPNPs, or RDLPNPs (200 μL), respectively, mice bearing Hela tumors were anesthetized and exposed to an 808 nm laser at the power density of 1.5 W cm^{-2}. Under irradiation, the tumor surface temperature of mice treated with RLPNPs or RDLPNPs increased from ~30 to ~55 ℃ within 5 min, whereas the temperature of the surrounding tissues increased by only 1.3 ℃ (Figure 5). In contrast, the tumor temperature of mice treated with PBS or free RAPA under the same NIR laser irradiation showed little change. These results revealed that our nanoparticles can rapidly raise the tumor temperature through the photothermal effect, which was able to kill both the tumor cells and tumor vasculature endothelial cells.

3.5. In Vivo Combinatory Antitumor Activity

Histopathology of various organs and tumor tissues according to H&E staining assay demonstrated that RDLPNPs plus NIR irradiation selectively destroyed the tumor cells without causing noticeable organ damage (Figure 6a and Figure S9).

To further evaluate the antitumor efficacy of our nanoparticles, the tumor volume and overall survival of the tumor-bearing mice were assessed (Figure 6b). The control groups (PBS and free RAPA) exhibited rapid increase in tumor volume and early death as a function of time. Compared with free RAPA, RDLPNPs possessed prolonged survival time, with the gentler growth in tumor volume, although their dose

of RAPA was self-same. In addition, DLPNPs plus NIR laser experienced better antitumor efficacy than that of RDLPNPs alone. As expected, RDLPNPs plus NIR laser performed the best antitumor efficiency with gradual decrease in tumor volume, and 80% survival rate up to 48 days, owing to the combination effect of targeted drug delivery and PTT. Moreover, the tumors were completely eliminated, leaving the original tumor site with black scars on day ten after treated with RDLPNPs plus NIR laser (Figure 6c). These results demonstrated that RDLPNPs based combinational anti-angiogenesis and PTT had superior antitumor therapeutic efficacy to either individual therapy.

3.6. In Vivo Antiangiogenesis Effect and Normalized Tumor Vessels

Angiogenesis, the sprouting of new blood vessels from existing parent ones, is crucial for tumor growth, evasion and metastasis [55]. Hence, it plays a key role in the control of tumor progression and become a target to inhibit tumor growth [56]. Unlike the normal blood vessels, the constitute of tumor vasculature is abnormal, resulting in the formation of physiological barriers which hinder the delivery of therapeutic drugs into tumors [57]. Therefore, antiangiogenic imbalances in the tumor results in tumor vasculature normalization and thus improves nanoparticle delivery and accumulation in the tumor [54]. Combination of PTT and chemotherapy during the vascular normalization also exhibits synergistic effects.

To evaluate the anti-angiogenic activity and distribution of RDLPNPs in the Hela tumor, blood vessels were stained by a CD-31 antibody (red color). PBS, free RAPA, DLPNPs or RDLPNPs was injected following the corresponding therapy experiments,

and the mice were sacrificed 24 h post intravenous administration (NIR laser was irritated at 6 h). As shown in Figure 7, mice treated with RDLPNPs with or without NIR laser irradiation resulted in significant increase of nanoparticles accumulation as well as significant decrease in the number of blood vessels in the tumor site. However, the number of tumor blood vessels in the mice receiving DLPNPs plus NIR laser treatment had little changes. Moreover, the blood vessel normalization was observed in the groups treated with RAPA, which was consistent with the previous reports [46, 58, 59]. Normalization might enhance transvascular flux and improve the delivery of nanoparticles to the tumor. To characterize blood flow, the blood vessel area was quantified by the ImageJ. RDLPNPs with or without NIR laser significantly re-expanded the microvasculature and increased the vessel area by approximately 2.9- and 3.8-fold over the PBS control group, respectively. However, DLPNPs employing NIR laser without RAPA did not exhibit marked blood vessel normalization. These results demonstrated that RDLPNPs under the NIR laser effectively ablated the tumor vasculature and significantly improved nanoparticles delivery into the tumor.

4. Conclusion

In conclusion, we have successfully designed and prepared a multifunctional RAPA/DiR loaded lipid-conducted polymer hybrid nanoparticle system, RDLPNPs. It can both effectivly shutdown tumor blood vessels by RAPA and ablate tumor cells through FRET enhanced PTT. Notably, PANI as a receptor of FRET can effectively convert the NIRF energy from the donor DiR resulting in improved PTT efficacy. RDLPNPs selectively accumulated in tumor sites via the active targeting effect in the

presence of FA ligand, which can be monitored by both fluorescence and photoacoustic imaging. The RAPA release to the intratumoral cells was subsequently triggered by the enhanced photothermal effect after laser irradiation. These results suggested that RDLPNP was a promising photothermal drug delivery nanosystem via an FRET effect, which provided a new strategy to enhance photothermal efficiency for superior imaging-guided chemo-photothermal therapy.

Acknowledgments

National Natural Science Foundation of China (81503016), the Application Foundation and Cutting-edge Technologies Research Project of Tianjin (Young Program) (15JCQNJC13800), and the National Basic Research Project (973 Program) of China (2014CB932200) are acknowledged for financial support. We would like to thank King's College London – K.C. Wong Postdoctoral Fellowships in supporting Dr Nan Li to carry out this research program. We thank Associate Professor Jun Dai for providing us the Hela cells.

References

[1] C. Wang, H. Xu, C. Liang, Y. Liu, Z. Li, G. Yang, L. Cheng, Y. Li, Z. Liu, Iron Oxide @ Polypyrrole Nanoparticles as a Multifunctional Drug Carrier for Remotely Controlled Cancer Therapy with Synergistic Antitumor Effect, ACS Nano, 7 (2013) 6782-6795.

[2] X. Huang, I.H. El-Sayed, W. Qian, M.A. El-Sayed, Cancer Cell Imaging and Photothermal Therapy in the Near-Infrared Region by Using Gold Nanorods, J. Am. Chem. Soc. 128 (2006) 2115-2120.

[3] D.P. O'Neal, L.R. Hirsch, N.J. Halas, J.D. Payne, J.L. West, Photo-thermal tumor ablation in

mice using near infrared-absorbing nanoparticles, Cancer Lett. 209 (2004) 171-176.

[4] P. Rai, S. Mallidi, X. Zheng, R. Rahmanzadeh, Y. Mir, S. Elrington, A. Khurshid, T. Hasan, Development and applications of photo-triggered theranostic agents, Adv. Drug Delivery Rev. 62 (2010) 1094-1124.

[5] E. Kim, J. Yang, J. Choi, J.S. Suh, Y.M. Huh, S. Haam, Synthesis of gold nanorod-embedded polymeric nanoparticles by a nanoprecipitation method for use as photothermal agents, Nanotechnology 20 (2009) 365602.

[6] Y. Wang, K.C.L. Black, H. Luehmann, W. Li, Y. Zhang, X. Cai, D. Wan, S.Y. Liu, M. Li, P. Kim, Z.Y. Li, L.V. Wang, Y. Liu, Y. Xia, Comparison Study of Gold Nanohexapods, Nanorods, and Nanocages for Photothermal Cancer Treatment, ACS Nano 7 (2013) 2068-2077.

[7] Z. Chen, Q. Wang, H. Wang, L. Zhang, G. Song, L. Song, J. Hu, H. Wang, J. Liu, M. Zhu, D. Zhao, Ultrathin PEGylated $W_{18}O_{49}$ Nanowires as a New 980 nm-Laser-Driven Photothermal Agent for Efficient Ablation of Cancer Cells In Vivo, Adv. Mater. 25 (2013) 2095-2100.

[8] L. Cheng, J. Liu, X. Gu, H. Gong, X. Shi, T. Liu, C. Wang, X. Wang, G. Liu, H. Xing, W. Bu, B. Sun, Z. Liu, PEGylated WS_2 Nanosheets as a Multifunctional Theranostic Agent for in vivo Dual-Modal CT/Photoacoustic Imaging Guided Photothermal Therapy, Adv. Mater. 26 (2014) 1886-1893.

[9] Q. Tian, M. Tang, Y. Sun, R. Zou, Z. Chen, M. Zhu, S. Yang, J. Wang, J. Wang, J. Hu, Hydrophilic Flower-Like CuS Superstructures as an Efficient 980 nm Laser-Driven Photothermal Agent for Ablation of Cancer Cells, Adv. Mater. 23 (2011) 3542-3547.

[10] Z. Zha, X. Yue, Q. Ren, Z. Dai, Uniform Polypyrrole Nanoparticles with High Photothermal

Conversion Efficiency for Photothermal Ablation of Cancer Cells, Adv. Mater. 25 (2013) 777-782.

[11] M. Lin, C. Guo, J. Li, D. Zhou, K. Liu, X. Zhang, T. Xu, H. Zhang, L. Wang, B. Yang, Polypyrrole-Coated Chainlike Gold Nanoparticle Architectures with the 808 nm Photothermal Transduction Efficiency up to 70%, ACS Appl. Mater. Interfaces 6 (2014) 5860-5868.

[12] J. Li, B. Arnal, C.W. Wei, J. Shang, T.M. Nguyen, M. O'Donnell, X. Gao, Magneto-Optical Nanoparticles for Cyclic Magnetomotive Photoacoustic Imaging, ACS NANO, 9 (2015) 1964-1976.

[13] J. Ge, Q. Jia, W. Liu, L. Guo, Q. Liu, M. Lan, H. Zhang, X. Meng, P. Wang, Red-Emissive Carbon Dots for Fluorescent, Photoacoustic, and Thermal Theranostics in Living Mice, Adv. Mater. 27 (2015) 4169-4177.

[14] M. Guo, J. Huang, Y. Deng, H. Shen, Y. Ma, M. Zhang, A. Zhu, Y. Li, H. Hui, Y. Wang, X. Yang, Z. Zhang, H. Chen, pH-Responsive Cyanine-Grafted Graphene Oxide for Fluorescence Resonance Energy Transfer-Enhanced Photothermal Therapy, Adv. Funct. Mater. 25 (2015) 59-67.

[15] H. Gong, L. Cheng, J. Xiang, H. Xu, L. Feng, X. Shi, Z. Liu, Near-Infrared Absorbing Polymeric Nanoparticles as a Versatile Drug Carrier for Cancer Combination Therapy, Adv. Funct. Mater. 23 (2013) 6059-6067.

[16] S. Sharifi, S. Behzadi, S. Laurent, M.L. Forrest, P. Stroeve, M. Mahmoudi, Toxicity of nanomaterials, Chem. Soc. Rev. 41 (2012) 2323-2343.

[17] S. Virji, R.B. Kaner, B.H. Weiller, Hydrazine Detection by Polyaniline Using Fluorinated

Alcohol Additives, Chem. Mater. 17 (2005) 1256-1260.

[18] D. Li, J. Huang, R.B. Kaner, Polyaniline Nanofibers: A Unique Polymer Nanostructure for Versatile Applications, Acc. Chem. Res. 42 (2009) 135-145.

[19] A.J. Heeger, Semiconducting and Metallic Polymers: The Fourth Generation of Polymeric Materials (Nobel Lecture), Angew. Chem. Int. Ed. 40 (2001) 2591-2611.

[20] J. Shi, Y. Chen, Q. Wang, Y. Liu, Construction and Efficient Radical Cation Stabilization of Cyclodextrin/Aniline Polypseudorotaxane and Its Conjugate with Carbon Nanotubes, Adv. Mater. 22 (2010) 2575-2578.

[21] J. Yang, J. Choi, D. Bang, E. Kim, E. Lim, H. Park, J. Suh, K. Lee, K. Yoo, E. Kim, Y. Huh, S. Haam, Convertible organic nanoparticles for near-infrared photothermal ablation of cancer cells, Angew. Chem. Int. Ed. 50 (2011) 461-464.

[22] J. Zhou, Z. Lu, X. Zhu, X. Wang, Y. Liao, Z. Ma, F. Li, NIR photothermal therapy using polyaniline nanoparticles, Biomaterials 34 (2013) 9584-9592.

[23] C. Hsiao, E. Chuang, H. Chen, D. Wan, C. Korupalli, Z. Liao, Y. Chiu, W. Chia, K. Lin, H. Sung, Photothermal tumor ablation in mice with repeated therapy sessions using NIR-absorbing micellar hydrogels formed in situ, Biomaterials 56 (2015) 26-35.

[24] B.P. Jiang, L. Zhang, Y. Zhu, et al. Water-soluble hyaluronic acid–hybridized polyaniline nanoparticles for effectively targeted photothermal therapy, J. Mater. Chem. B 3 (2015) 3767-3776.

[25] P. Huang, C. Xu, J. Lin, C. Wang, X. Wang, C. Zhang, X. Zhou, S. Guo, D. Cui, Folic Acid-conjugated Graphene Oxide loaded with Photosensitizers for Targeting Photodynamic Therapy, Theranostics 1 (2011) 240-250.

[26] B. Tian, C. Wang, S. Zhang, L. Feng, Z. Liu, Photothermally enhanced photodynamic therapy delivered by nano-graphene oxide, ACS Nano 5 (2011) 7000-7009.

[27] D.K. Lim, A. Barhoumi, R.G. Wylie, G. Reznor, R.S. Langer, D.S. Kohane, Enhanced Photothermal Effect of Plasmonic Nanoparticles Coated with Reduced Graphene Oxide, Nano Lett. 13 (2013) 4075-4079.

[28] A.F. Zedan, S. Moussa, J. Terner, G. Atkinson, M.S. El-Shall, Ultrasmall Gold Nanoparticles Anchored to Graphene and Enhanced Photothermal Effects by Laser Irradiation of Gold Nanostructures in Graphene Oxide Solutions, ACS Nano 7 (2013) 627-636.

[29] H. Hong, Y. Zhang, J.W. Engle, T.R. Nayak, C.P. Theuer, R.J. Nickles, T.E. Barnhart, W. Cai, In vivo targeting and positron emission tomography imaging of tumor vasculature with 66Ga-labeled nano-graphene, Biomaterials 33 (2012) 4147-4156.

[30] H. Hong, K. Yang, Y. Zhang, J.W. Engle, L. Feng, Y. Yang, T.R. Nayak, S. Goel, J. Bean, C.P. Theuer, T.E. Barnhart, Z. Liu, W. Cai, In Vivo Targeting and Imaging of Tumor Vasculature with Radiolabeled, Antibody-Conjugated Nanographene, ACS Nano 6 (2012) 2361-2370.

[31] K. Yang, L.L. Hu, X.X. Ma, S.Q. Ye, L. Cheng, X.Z. Shi, C.H. Li, Y.G. Li, Z. Liu, Multimodal Imaging Guided Photothermal Therapy using Functionalized Graphene Nanosheets Anchored with Magnetic Nanoparticles, Adv. Mater. 24 (2012) 1868-1872.

[32] X.X. Ma, H.Q. Tao, K. Yang, L.Z. Feng, L. Cheng, X.Z. Shi, Y.G. Li, L. Guo, Z. Liu, A functionalized graphene oxide-iron oxide nanocomposite for magnetically targeted drug delivery, photothermal therapy, and magnetic resonance imaging, Nano Res. 5 (2012) 199-212.

[33] S. Kanakia, J.D. Toussaint, S.M. Chowdhury, G. Lalwani, T. Tembulkar, T. Button, K.R.

Shroyer, W. Moore, B. Sitharaman, Physicochemical characterization of a novel graphene-based magnetic resonance imaging contrast agent, Int. J. Nanomed. 8 (2013) 2821-2833.

[34] X. Shi, H. Gong, Y. Li, C. Wang, L. Cheng, Z. Liu, Graphene-based magnetic plasmonic nanocomposite for dual bioimaging and photothermal therapy, Biomaterials 34 (2013) 4786-4793.

[35] L. Nie, S. Wang, X. Wang, P. Rong, A. Bhirde, Y. Ma, G. Liu, P. Huang, G. Lu, X. Chen, In Vivo Volumetric Photoacoustic Molecular Angiography and Therapeutic Monitoring with Targeted Plasmonic Nanostars, Small 10 (2014) 1585-1593.

[36] D. Razansky, C. Vinegoni, V. Ntziachristos, Multispectral photoacoustic imaging of fluorochromes in small animals, Opt. Lett. 32 (2007) 289-293.

[37] Y. Zhang, X. Cai, Y. Wang, C. Zhang, L. Li, S. Choi, L.V. Wang, Y. Xia, Noninvasive Photoacoustic Microscopy of Living Cells in Two and Three Dimensions through Enhancement by a Metabolite Dye, Angew. Chem. Int. Ed. 123 (2011) 7497-7501.

[38] X.H. Zheng, D. Xing, F.F. Zhou, B.Y. Wu, W.R. Chen, Indocyanine green-containing nanostructure as near infrared dual-functional targeting probes for optical imaging and photothermal therapy, Mol. Pharm. 8 (2011) 447-456.

[39] F.P. Gao, Y.X. Lin, L.L. Li, Y. Liu, U. Mayerhoffer, P. Spenst, J.G. Su, J.Y. Li, F. Wurthner, H. Wang, Supramolecular adducts of squaraine and protein for noninvasive tumor imaging and photothermal therapy in vivo, Biomaterials 35 (2014) 1004-1014.

[40] M.B. Zheng, C.X. Yue, Y.F. Ma, P. Gong, P.F. Zhao, C.F. Zheng, Z.H. Sheng, P.F. Zhang, Z.H. Wang, L.T. Cai, Single-step assembly of DOX/ICG loaded lipid–polymer nanoparticles for

highly effective chemo-photothermal combination therapy, ACS Nano 7 (2013) 2056-2067.

[41] L. Cheng, W. He, H. Gong, C. Wang, Q. Chen, Z. Cheng, Z. Liu, PEGylated Micelle Nanoparticles Encapsulating a Non-Fluorescent Near-Infrared Organic Dye as a Safe and Highly-Effective Photothermal Agent for In Vivo Cancer Therapy, Adv. Funct. Mater. 23 (2013) 5893-5902.

[42] F.M. Youniss, G. Sundaresan, L.J. Graham, L. Wang, C.R. Berry, G.K. Dewkar, P. Jose, H.D. Bear, J. Zweit, Near-Infrared Imaging of Adoptive Immune Cell Therapy in Breast Cancer Model Using Cell Membrane Labeling, PLOS One 9 (2014) e109162.

[43] H. Cho, G.L. Indig, J. Weichert, H. Shin, G.S. Kwon, In vivo cancer imaging by poly(ethylene glycol)-b-poly(ε -caprolactone) micelles containing a near-infrared probe, Nanomedicine 8 (2012) 228-236.

[44] X. He, X. Bao, H. Cao, Z. Zhang, Q. Yin, W. Gu, L. Chen, H. Yu, Y. Li, Tumor-Penetrating Nanotherapeutics Loading a Near-Infrared Probe Inhibit Growth and Metastasis of Breast Cancer, Adv. Funct. Mater. 25 (2015) 2831–2839.

[45] X. Wang, J. Zhang, W. Zou, R. Wang, Facile synthesis of polyaniline/carbon dot nanocomposites and their application as a fluorescent probe to detect mercury, RSC Adv. 5, (2015) 41914-41919.

[46] J. Yang, J. Choi, D. Bang, E. Kim, E. Lim, H. Park, J. Suh, K. Lee, K. Yoo, E. Kim, Y. Huh, S. Haam, Convertible organic nanoparticles for near-infrared photothermal ablation of cancer cells, Angew. Chem. Int. Ed. 50 (2011) 461-464.

[47] P.P. Provenzano, C. Cuevas, A.E. Chang, V.K. Goel, D.D. Von Hoff, S.R. Hingorani, Enzymatic Targeting of the Stroma Ablates Physical Barriers to Treatment of Pancreatic

Ductal Adenocarcinoma, Cancer Cell 21 (2012) 418-429.

[48] W. Dai, F. Yang, L. Ma, Y. Fan, B. He, Q. He, X. Wang, H, Zhang, Q. Zhang, Combined mTOR inhibitor rapamycin and doxorubicin-loaded cyclic octapeptide modified liposomes for targeting integrin α3 in triple-negative breast cancer, Biomaterials 35 (2014) 5347-5358.

[49] M. Shah, M.C. Edman, S.R. Janga, et al. A rapamycin-binding protein polymer nanoparticle shows potent therapeutic activity in suppressing autoimmune dacryoadenitis in a mouse model of Sjögren's syndrome, J. Control. Release 171 (2013) 269-279.

[50] W. Tai, Z. Chen, A. Barve, et al. A novel rapamycin-polymer conjugate based on a new poly (ethylene glycol) multiblock copolymer. Pharmaceutical research 31 (2014), 706-719.

[51] D.A. Mannock, M.G.K. Benesch, R.N.A.H. Lewis, R.N. McElhaney, A comparative calorimetric and spectroscopic study of the effects of cholesterol and of the plant sterols β-sitosterol and stigmasterol on the thermotropic phase behavior and organization of dipalmitoylphosphatidylcholine bilayer membranes, BBA. Biomembranes 1848 (2015) 1629-1638.

[52] R. Lv, P. Yang, F. He, S. Gai, C. Li, Y. Dai, G. Yang, J. Lin, A yolk-like multifunctional platform for multimodal imaging and synergistic therapy triggered by a single near-infrared light, ACS Nano 9 (2015) 1630-1647.

[53] B. Tian, C. Wang, S. Zhang, L.Z. Feng, Z. Liu, Photothermally enhanced photodynamic therapy delivered by nano-graphene oxide, ACS Nano 5 (2011) 7000-7009.

[54] S.P. Sherlock, S.M. Tabakman, L.M. Xie, H.J. Dai, Photothermally Enhanced Drug Delivery by Ultrasmall Multifunctional FeCo/Graphitic Shell Nanocrystals, ACS Nano 5 (2011) 1505-1512.

[55] S.M. Weis, D.A. Cheresh, Tumor angiogenesis: molecular pathways and therapeutic targets, Nat. Med. 17 (2011) 1359-1370.

[56] P. Carmeliet, R.K. Jain, Angiogenesis in cancer and other diseases, Nature 407 (2000) 249-257.

[57] R.K. Jain, Normalization of tumor vasculature: an emerging concept in antiangiogenic therapy, Science 307 (2005) 58-62.

[58] S. Guo, C.M. Lin, Z. Xu, L. Miao, Y. Wang, L. Huang, Co-delivery of Cisplatin and Rapamycin for Enhanced Anticancer Therapy through Synergistic Effects and Microenvironment Modulation, ACS Nano 8 (2014) 4996-5009.

[59] E. Fokas, J.H. Im, S. Hill, S. Yameen, M. Stratford, J. Beech, W. Hackl, S.M. Maira, E.J. Bernhard, W.G. McKenna, et al. Dual inhibition of the Pi3k/Mtor pathway increases tumor radiosensitivity by normalizing tumor vasculature, Cancer Res. 72 (2012) 239-248.

Figures

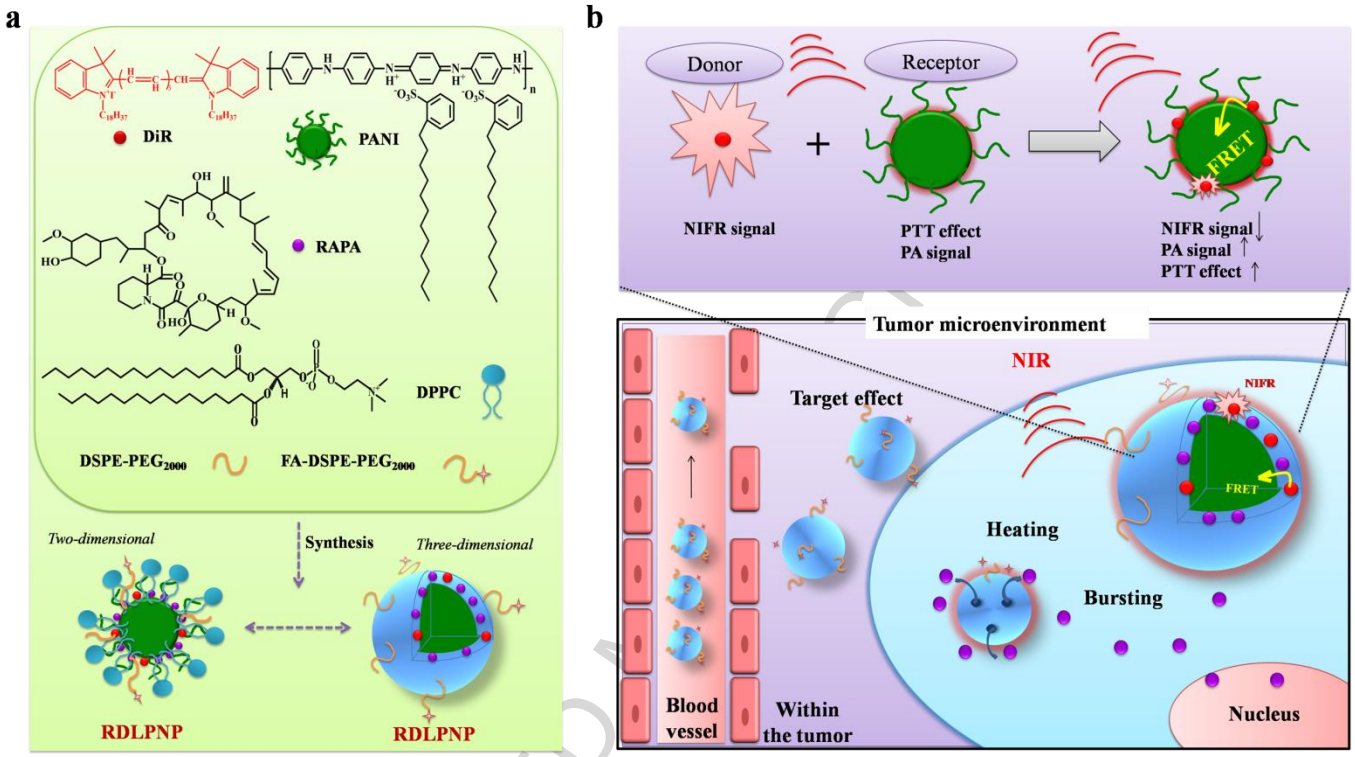

Scheme 1. (a) Construction of tumor-targeting RAPA/DiR loaded lipid-polyaniline hybrid nanoparticle system, RDLPNP. (b) Schematic illustration of RDLPNPs exhibiting photoacoustic and fluorescence imaging guided combination therapy of antiangiogenesis and enhanced photothermal performance mediated by FRET.

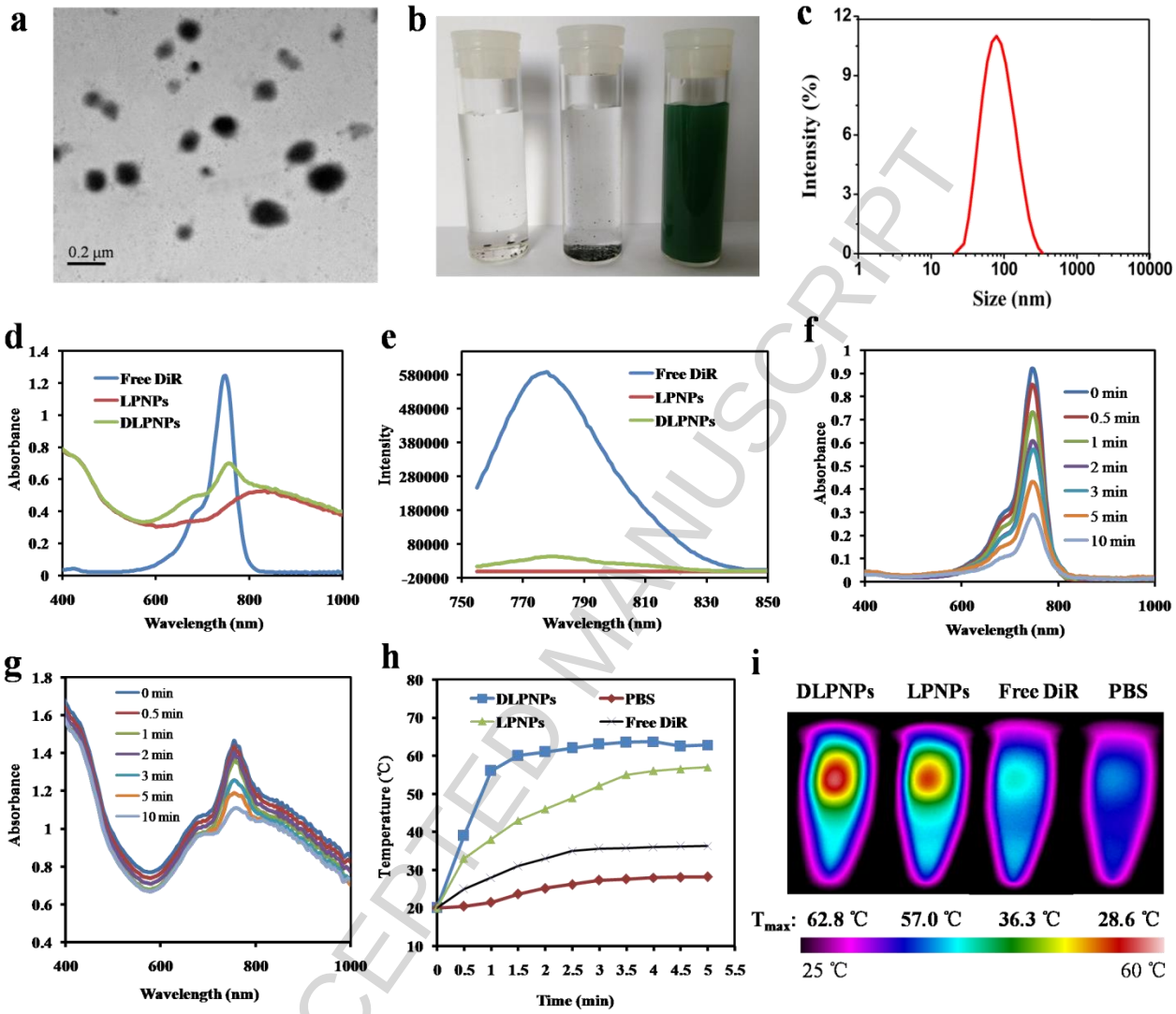

Figure 1. (a) TEM image of DLPNPs. (b) Photographs of DiR, PANI and DLPNPs dispersed in PBS (pH 7.4). (c) Size distribution of DLPNPs. (d) UV-Vis absorption spectra of free DiR dissolved in methanol, LPNPs or DLPNPs dispersed in water. (e) Fluorescence spectra of DiR, LPNPs, and DLPNPs in the aqueous solution. (f) UV-Vis spectra of free DiR exposed to 1.5 W cm^{-2} 808 nm photoirradiation at different time, respectively. (g) UV-Vis spectra of DLPNPs in aqueous solution under 1.5 W cm^{-2} photoirradiation at different time, respectively. (h) Temperature evolution curves of PBS, aqueous solution of DLPNPs, LPNPs, and free DiR dissolved in methanol over a period of 5 min following exposure to the NIR laser (808 nm, 1.5 W cm^{-2}). (i) Photothermal images of PBS, aqueous solution of DLPNPs, LPNPs, and free DiR dissolved in methanol over following exposure to the NIR laser (808 nm, 1.5 W $cm^{-2,}$ 5 min).

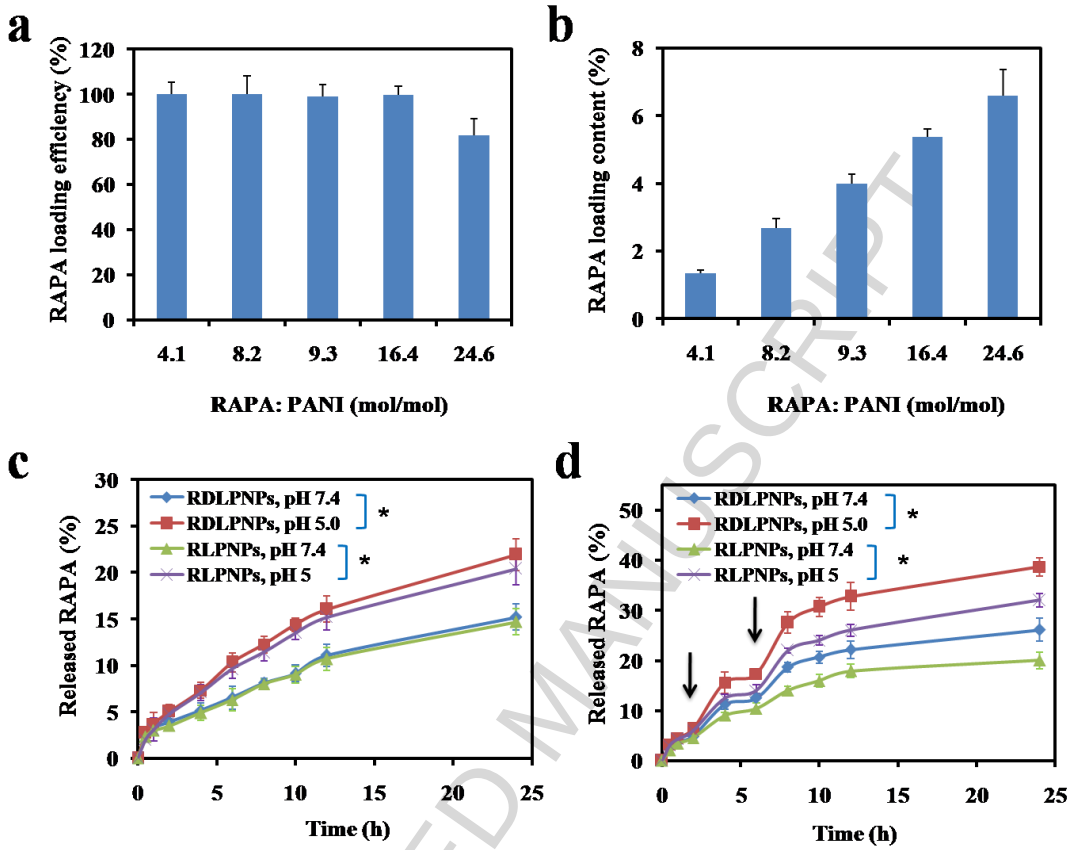

Figure 2. (a) Loading efficiency of RAPA in the RDLPNPs at different RAPA concentrations. (b) Loading content of RAPA in the RDLPNPs at different RAPA concentrations. (c) RAPA release from RDLPNPs or RLPNPs over time in buffers at the two different pH values indicated. (d) NIR-triggered release of RAPA from RDLPNPs or RLPNPs. The samples at two pH values were irradiated with an NIR laser (1.5 W cm^{-2}) for 3 min at different time points indicated by the arrows. The data are presented as the mean ± SD (n = 3), *P < 0.05.

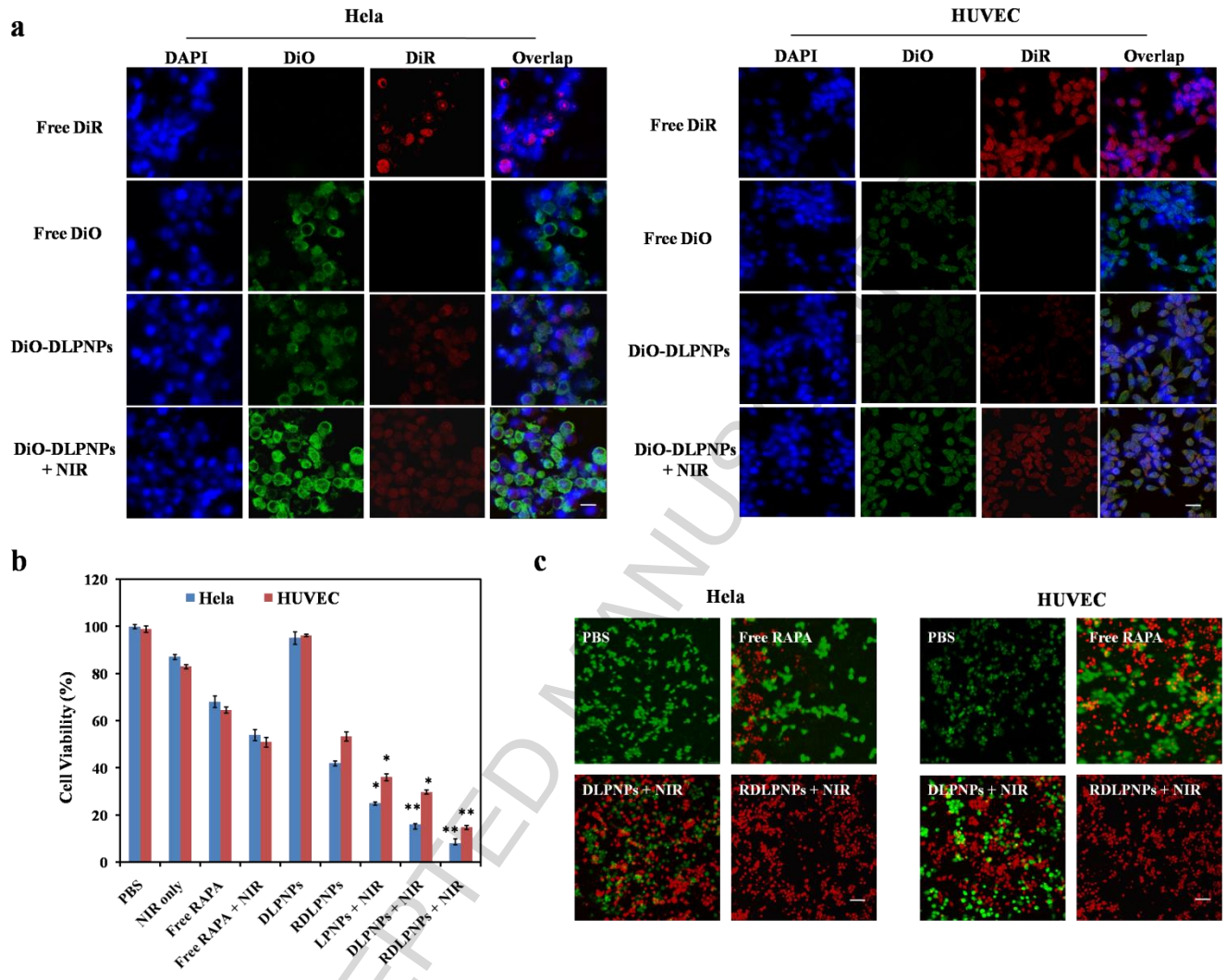

Figure 3. (a) Confocal images of Hela cells and HUVECs incubated with free DiO, free DiR, or DiO-DLPNPs with or without an NIR laser (808 nm, 1.5 W cm^{-2}). Blue colors in those images represent DAPI-stained nuclear fluorescence. Green colors represent DiO fluorescence, which imitates the RAPA. Red colors represent DiR fluorescence. The scale bars are 25 μm in all confocal images. (b) Relative viabilities of Hela cells and HUVECs after incubation with PBS, free RAPA, LPNPs, DLPNPs, or RDLPNPs with or without laser irradiation (808 nm, 1.5 W cm^{-2}). The data are presented as the mean ± SD (n = 3), *P < 0.05, **P < 0.01. (c) Confocal fluorescence images of Calcein AM/PI stained Hela cells and HUVECs incubated with PBS, free RAPA, DLPNPs plus NIR laser, or RDLPNP plus NIR laser, respectively. The scale bars are 100 μm in all confocal images.

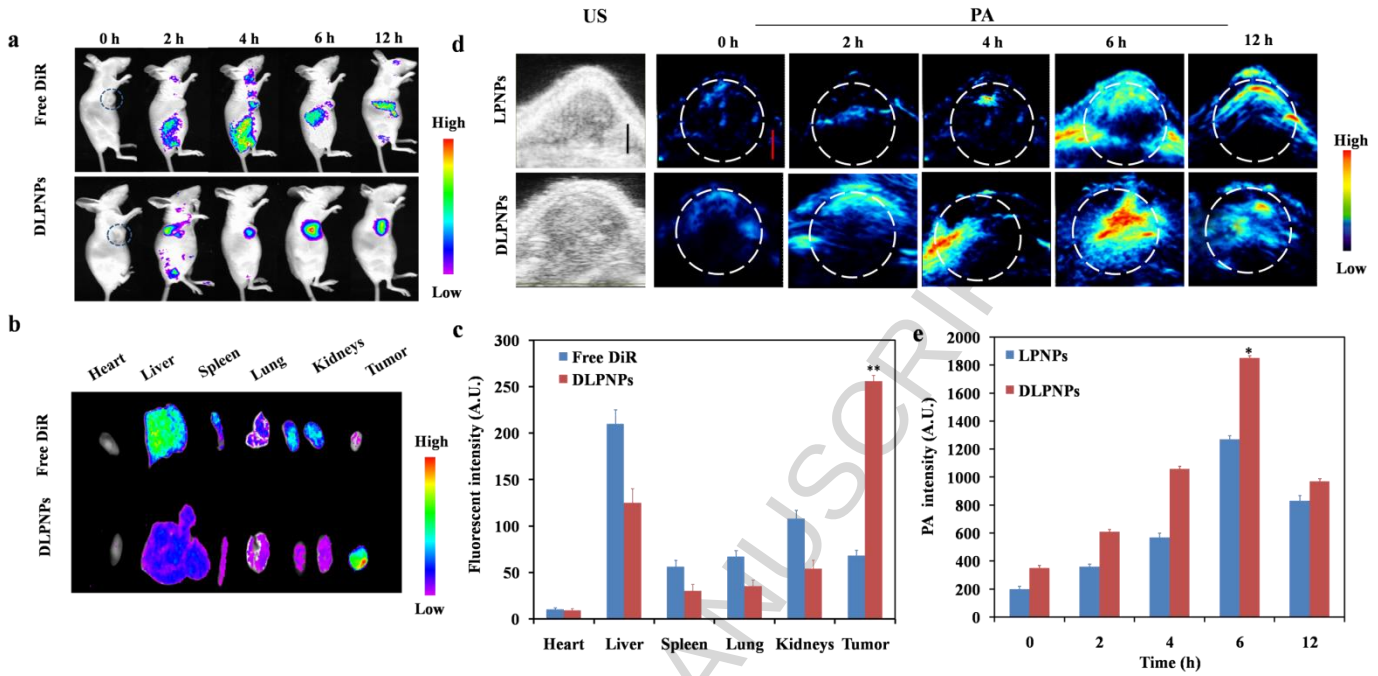

Figure 4. (a) In vivo fluorescence imaging of subcutaneous Hela tumor-bearing Balb/c mice after intravenous injection with free DiR or DLPNPs. (b) The fluorescence imaging of dissected organs after intravenous injection with free DiR or DLPNPs. (c) Semi-quantitative of intensity of different organs and tumor. The data are presented as the mean ± SD (n = 3). **P < 0.01, significantly higher than that of free DiR. (d) Ultrasound (US) images and photoacoustic images of Hela tumor-bearing mice intravenously DLPNPs or LPNPs. The tumors are highlighted by white circle. The scale bars are 4 mm in the images. (e) Photoacoustic intensity of tumour tissues at different time points. The data are presented as the mean ± SD (n = 3), *P < 0.05.

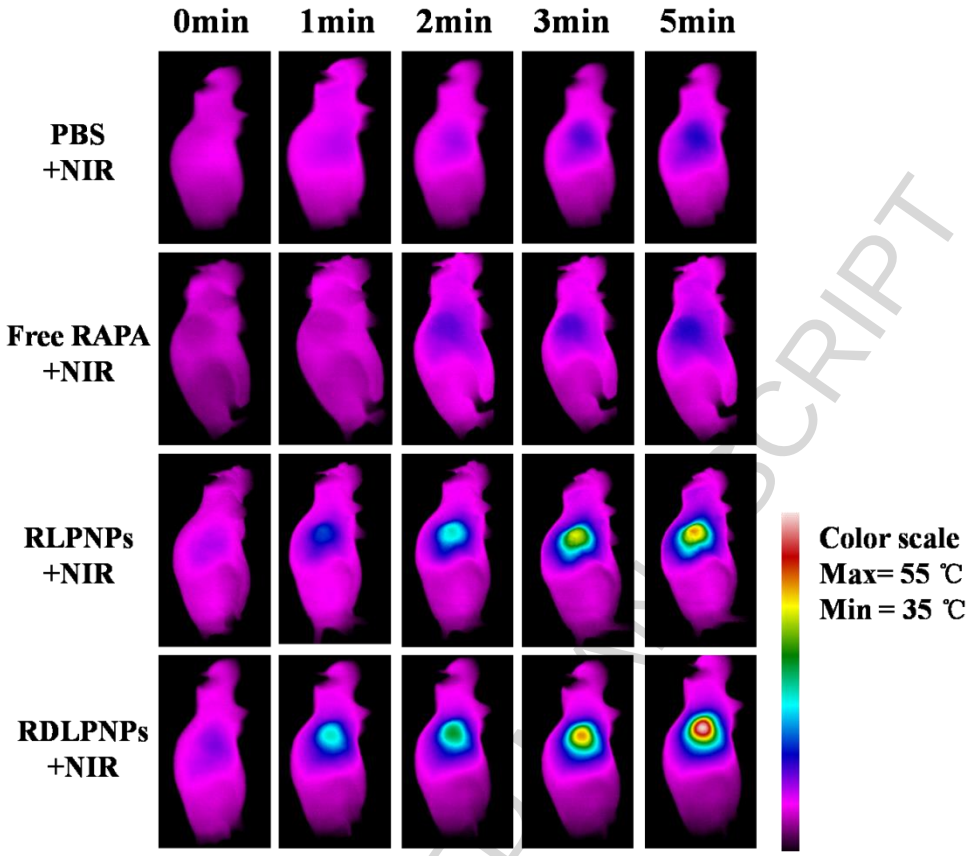

Figure 5. Photothermal images of tumor-bearing mice exposed to the NIR laser (808 nm, 1.5 W cm^{-2}, 5 min) after intravenous injection with PBS, free RAPA, RLPNPs, or RDLPNPs, respectively.

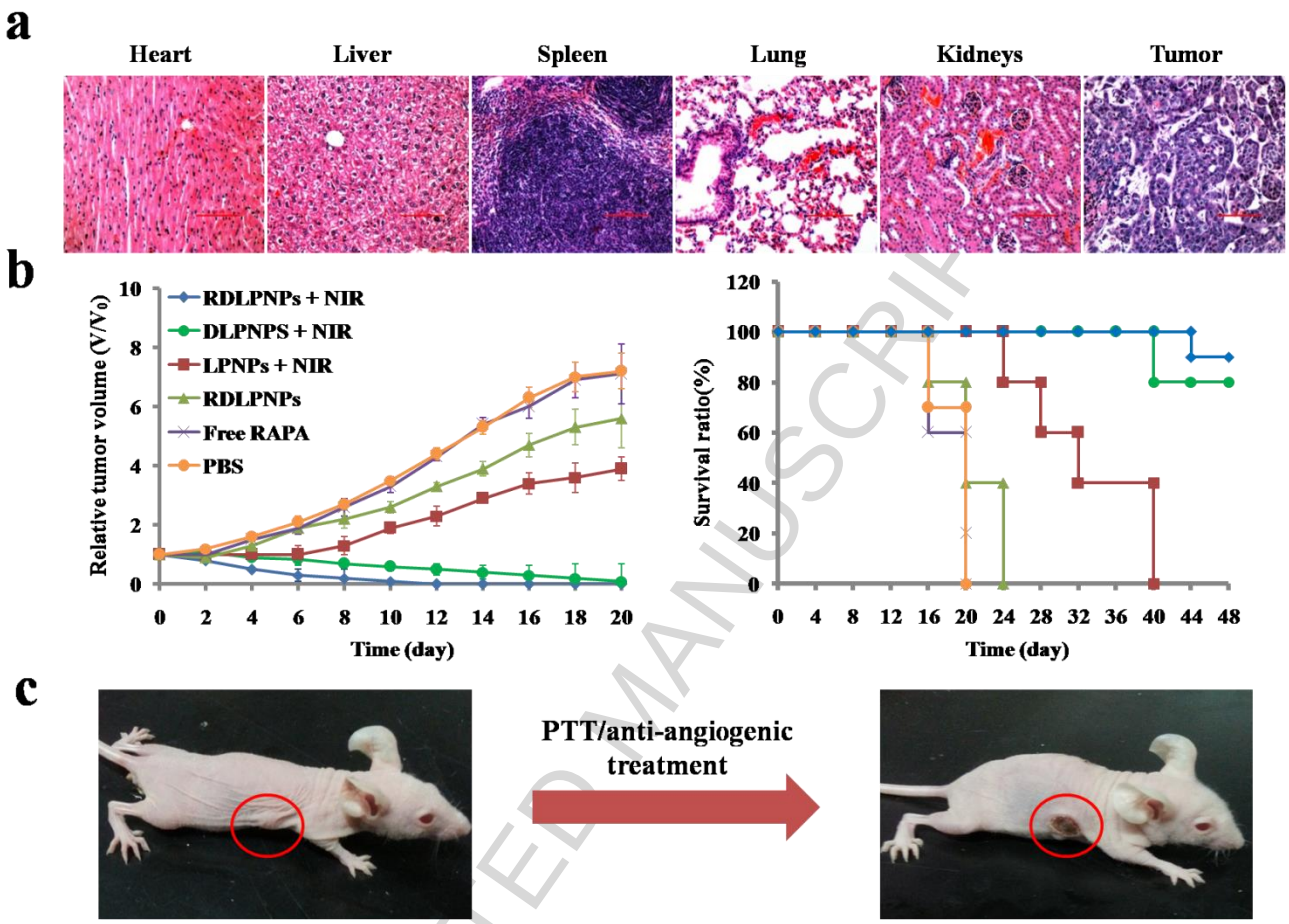

Figure 6. (a) H&E-stained different organ slices collected from mice after treatments with RLPNPs exposed to NIR laser (808 nm, 1.5 W cm^{-2}). The scale bars are 100 μm. (b) Growth of Hela tumors in different groups of mice after treatment. The relative tumor volumes were normalized to their initial sizes on the left figure. Survival curves of mice after various treatments as indicated on the right figure. RDLPNPs-injected mice after PTT treatment showed 80% survival ratio over 48 days. (c) Representative photos of a RDLPNPs-injected mouse at day 0 before PTT treatment and at day 10 after treatment.

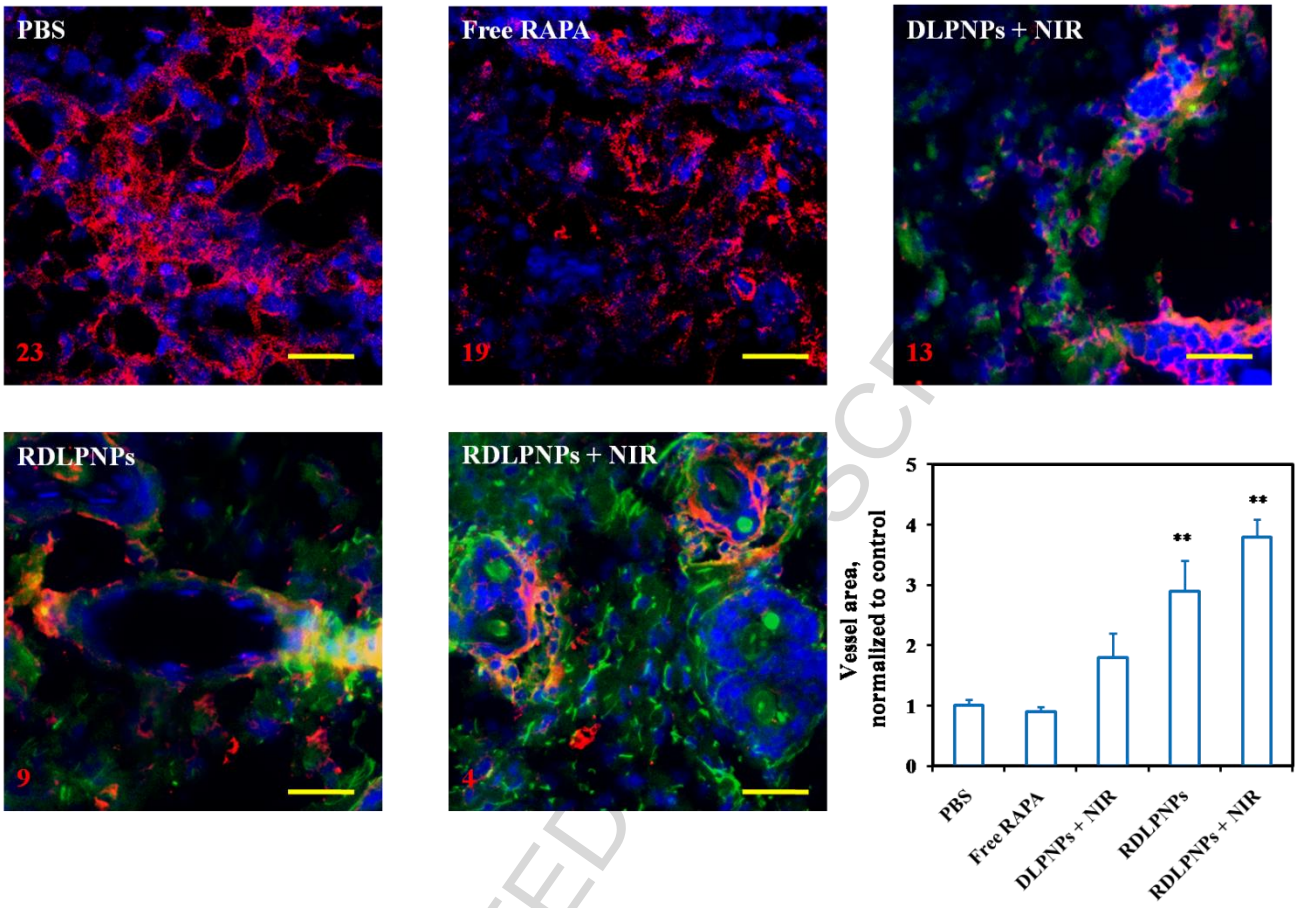

Figure 7. Antiangiogenesis effect and distribution of various formulations on the Hela xenograft tumor were investigated by CD-31 staining (red). Nuclei were stained blue. Green colors represent the fluorescence of DiR. The number denotes the average number of CD-31 positive vessels per microscopic field. Vessel area, quantified using ImageJ, was normalized to a PBS treated control. Five randomly selected microscopic fields were quantitatively analyzed on ImageJ. The data are presented as the mean ± SD (n = 3), **P < 0.01. The scale bar represents 50 μm.

Graphical Abstract